Title

A nondestructive method for the pretension detection in membrane structures based on nonlinear vibration response to impact

Authors

Liu, Chang-Jiang
Todd, Michael D
Zheng, Zhou-Lian
et al.

A nondestructive method for the pretension detection in membrane structures based on nonlinear vibration response to impact

Chang-Jiang Liu[1,2], Michael D Todd[2], Zhou-Lian Zheng[3] and Yu-You Wu[4]

Abstract
The pretension of building membrane structures may relax over its service lifetime, which may cause engineering failure under external loads. Therefore, the pretension of building membrane structures should be monitored or estimated regularly to compare the actual pretension to its design pretension and then to adopt some strengthening measures to mitigate future problems. Based on the geometrically nonlinear vibration of a rectangular orthotropic membrane structure, a nondestructive detection method for monitoring its pretension is developed in this article. This method is achieved by impacting a low-velocity pellet onto the membrane surface to generate vibration and detecting its response amplitude. Then the detected amplitude is converted into a pretension estimate via a derived formula. In addition, experiments for three kinds of conventional membrane material (Heytex H5573, Xing Yi Da, and ZZF 3010) were carried out according to the theoretical idea. The experimental results proved this method is feasible and verified the theoretical derivation is reasonable.

Introduction

The application of membrane materials in modern building structures has been recently growing. Due to their architectural features, economy, and reduced weight, they are widely applied in large-scale stadia, airport terminals, department stores, and other large commercial buildings.[1–3] The tensile building membrane structure's stiffness is formed by applying pretension to the structure. This pretension value is the critical parameter that governs a number of structural failure modes, and monitoring it may provide safety assurance or suggest mitigation prior to catastrophic failure. However, monitoring such structures is still an unresolved issue in the field of membrane structure health monitoring.[4–7]

A monitoring strategy based on vibration response features has a rich history.[8] For example, Farrar et al.[9] introduced the four-part process of vibration-based structural damage identification in detail. Staszewski et al.[10] demonstrated that temperature and ambient vibrations can affect the performance of piezoelectric sensors employed in composite plate tests. Todd et al.[11] reported the development of fiber optic sensors for vibration-based structural health monitoring (SHM) applications. Then a novel feature extracted from a nonlinear time series is presented by Todd et al.[12] within the context of vibration-based damage detection in a system. Razi et al.[13] developed a vibration-based health monitoring (VBHM) strategy for detecting the loosening of bolts in a pipeline's bolted flange joint by numerical and experimental studies. Bao et al.[14] proposed a vibration-based integrated autoregressive moving average (ARMA) model algorithm that can be used for online SHM of offshore pipeline structures, as well as other civil structures. Sakaris et al.[15] presented a

[1]College of Environment and Civil Engineering, Chengdu University of Technology, Chengdu, China
[2]Department of Structural Engineering, University of California, San Diego, La Jolla, CA, USA
[3]College of Civil Engineering, Chongqing University, Chongqing, China
[4]Department of Buildings, Shenzhen Institute of Building Research, Shenzhen, China

Corresponding author:
Michael D Todd, Department of Structural Engineering, University of California, San Diego, La Jolla, CA 92093, USA.
Email: mdtodd@ucsd.edu

vibration-based strategy for damage precise localization on three-dimensional structures through the vector version of an advanced Functional Model–Based Method. Valdés-González et al.[16] presented an experimental study conducted on a two-story reinforced concrete frame for its seismic damage detection using ambient and forced vibration records. Soyoz and Feng[17] developed an extended Kalman filtering (EKF) method for instantaneously identifying elemental stiffness values of a structure during damaging seismic events based on vibration measurement, and it was verified by a large-scale shaking table test of a three-bent concrete bridge model. Kim et al.[18] reported a study of a field experimental on a steel Gerber-truss bridge for damage detection utilizing vehicle-induced vibrations. Kopsaftopoulos and Fassois[19] carried out an experimental assessment of a sequential probability ratio test framework for vibration-based SHM. Mooney et al.[20] carried out experimental program to explore the efficacy of VBHM of earth structures. In addition to these studies, there are still many other reports about novel and unique VBHM strategies of metal, concrete, and earth structures.[21–28] However, there are few studies about the health monitoring of building membrane structures, and more specifically, the monitoring of membrane pretension.

Sun and colleagues[29–31] developed the Cable Analogy Method (CAM) for pretensioned structures. CAM is essentially the displacement method, and it uses cable theory to calculate membrane displacement, which is somewhat restrictive in both theoretical assumption and difficult to implement in practice. Zheng et al.[32] developed and verified a new method, the Ejection Method, where the objective was to eject a pellet onto the tensile membrane surface, measure the ejection and rebound velocity of the pellet and the amplitude of the membrane to obtain the pretension of the membrane structure. But this method requires three parameters. This increased the possibility of error and created some engineering difficulty in making the necessary measurements to implement the method.

Building upon the idea of the Ejection Method, this article developed a method that only requires one measurement parameter (the amplitude of the membrane $u_{\max}$) to obtain the pretension of the membrane structure. First, this article derives a model for the large-amplitude nonlinear vibration of an orthotropic membrane and then obtains a detection formula. Second, experiments on the three kinds of conventional membrane material (Heytex H5573, Xing Yi Da, and ZZF 3010) were carried out to show feasibility.

Fundamental approach

The basic idea is to exploit the membrane nonlinear vibration response resulting from a low-velocity impact. The response amplitude of the membrane ($u_{\max}$) will then be used to obtain the pretension of the membrane. The schematic diagram of the monitoring is shown in Figure 1.

In Figure 1, v_0 denotes the initial velocity of the pellet; a denotes the length of warp direction; b denotes the length of weft direction; N_{0x} and N_{0y} denote initial tension (pretension) in x and y direction, respectively; (x_0, y_0) denotes the center point of the membrane; and $u_{\max}$ denotes the maximum amplitude of the center point of the membrane.

According to the basic idea, based on the calculation of the nonlinear vibration response of the membrane under the impact loading, we may derive the relationship between the amplitude $u_{\max}$ and the pretension of the membrane. We assume that the vibration initiates when the membrane surface reaches its initial maximum displacement $u_{\max}$ after the impact interaction. Therefore, the vibration maybe treated as a free vibration with the initial condition of the lateral displacement of the center point, $u_{\max}$.
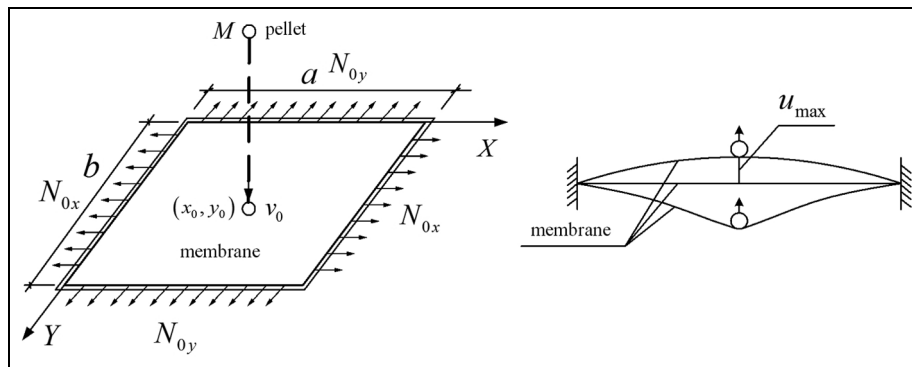

Figure 1. Schematic diagram of this method.

According to the Von Kármán's membrane large deflection theory and D'Alembert's principle,[34–36] the undamped vibration partial differential equation and consistency equation of orthotropic membrane are

$$\begin{cases} \rho \dfrac{\partial^2 w}{\partial t^2} - (N_x + N_{0x}) \dfrac{\partial^2 w}{\partial x^2} - (N_y + N_{0y}) \dfrac{\partial^2 w}{\partial y^2} - 2(N_{xy} + N_{0xy}) \dfrac{\partial^2 w}{\partial x \partial y} = 0 \\ \dfrac{1}{E_1 h} \dfrac{\partial^2 N_x}{\partial y^2} - \dfrac{\mu_2}{E_2 h} \dfrac{\partial^2 N_y}{\partial y^2} - \dfrac{\mu_1}{E_1 h} \dfrac{\partial^2 N_x}{\partial x^2} + \dfrac{1}{E_2 h} \dfrac{\partial^2 N_y}{\partial x^2} - \dfrac{1}{Gh} \dfrac{\partial^2 N_{xy}}{\partial x \partial y} = \left(\dfrac{\partial^2 w}{\partial x \partial y} \right)^2 - \dfrac{\partial^2 w}{\partial x^2} \dfrac{\partial^2 w}{\partial y^2} \end{cases} \quad (1)$$

where ρ denotes aerial density of membrane; N_x and N_y denote additional tension in x and y directions, respectively; N_{xy} denotes additional shear force; N_{0xy} denotes initial shear force; w denotes deflection $w(x, y, t)$; h denotes the membrane thickness; E_1 and E_2 denote Young's modulus in x and y directions, respectively; G denotes the shear modulus; and μ_1 and μ_2 denote Poisson's ratio in x and y directions, respectively.

Using the Airy stress function definition, we have

$$N_x = h \frac{\partial^2 \varphi}{\partial y^2}, N_y = h \frac{\partial^2 \varphi}{\partial x^2}, N_{xy} = -h \frac{\partial^2 \varphi}{\partial x \partial y}$$

and set

$$N_{0x} = h \cdot \sigma_{0x}, N_{0y} = h \cdot \sigma_{0y}, N_{0xy} = -h \cdot \sigma_{0xy}$$

where φ denotes stress function $\varphi(x, y, t)$; σ_{0x} and σ_{0y} denote initial tensile stress in x and y direction, respectively; and σ_{0xy} denotes initial shear stress.

The maximum vibration displacement of the membrane is much smaller than the boundary size, so the shearing actions among the membrane fibers are very small, and the effect of shearing stresses is thus assumed negligible. Therefore

$$N_{0xy} = -h \cdot \sigma_{0xy} = 0, N_{xy} = -h \frac{\partial^2 \varphi}{\partial x \partial y} = 0$$

and the governing equation (1) is simplified as follows

$$\frac{\rho}{h} \frac{\partial^2 w}{\partial t^2} - \left(\sigma_{0x} + \frac{\partial^2 \varphi}{\partial y^2} \right) \frac{\partial^2 w}{\partial x^2} - \left(\sigma_{0y} + \frac{\partial^2 \varphi}{\partial x^2} \right) \frac{\partial^2 w}{\partial y^2} = 0 \quad (2)$$

$$\frac{1}{E_1} \frac{\partial^4 \varphi}{\partial y^4} + \frac{1}{E_2} \frac{\partial^4 \varphi}{\partial x^4} = \left(\frac{\partial^2 w}{\partial x \partial y} \right)^2 - \frac{\partial^2 w}{\partial x^2} \frac{\partial^2 w}{\partial y^2} \quad (3)$$

The corresponding boundary conditions are expressed as follows

$$\begin{cases} w(0, y, t) = 0, \dfrac{\partial^2 w}{\partial x^2}(0, y, t) = 0 \\ w(a, y, t) = 0, \dfrac{\partial^2 w}{\partial x^2}(a, y, t) = 0 \end{cases}, \begin{cases} w(x, 0, t) = 0, \dfrac{\partial^2 w}{\partial y^2}(x, 0, t) = 0 \\ w(x, b, t) = 0, \dfrac{\partial^2 w}{\partial y^2}(x, b, t) = 0 \end{cases} \quad (4)$$

$$\begin{cases} \dfrac{\partial^2 \varphi}{\partial x^2}(0, y, t) = 0 \\ \dfrac{\partial^2 \varphi}{\partial x^2}(a, y, t) = 0 \end{cases}, \begin{cases} \dfrac{\partial^2 \varphi}{\partial y^2}(x, 0, t) = 0 \\ \dfrac{\partial^2 \varphi}{\partial y^2}(x, b, t) = 0 \end{cases}, \begin{cases} \dfrac{\partial^2 \varphi}{\partial x \partial y}(x, 0, t) = 0 \\ \dfrac{\partial^2 \varphi}{\partial x \partial y}(x, b, t) = 0 \end{cases}, \begin{cases} \dfrac{\partial^2 \varphi}{\partial x \partial y}(0, y, t) = 0 \\ \dfrac{\partial^2 \varphi}{\partial x \partial y}(a, y, t) = 0 \end{cases} \quad (5)$$

Separable functions that satisfy the boundary conditions (4) and (5) may be written as follows

$$w(x, y, t) = u(t) W(x, y) \quad (6)$$

$$\varphi(x, y, t) = U(t) \cdot \phi(x, y) \quad (7)$$

where $u(t)$ and $U(t)$ are unknown time-dependent functions. Substituting equations (6) and (7) into equation (3) yields

$$\left(\frac{1}{E_1} \frac{\partial^4 \phi(x, y)}{\partial y^4} + \frac{1}{E_2} \frac{\partial^4 \phi(x, y)}{\partial x^4} \right) \cdot U(t) = \left(\left(\frac{\partial^2 W(x, y)}{\partial x \partial y} \right)^2 - \frac{\partial^2 W(x, y)}{\partial x^2} \frac{\partial^2 W(x, y)}{\partial y^2} \right) u^2(t) \quad (8)$$

For compatibility in equation (8), we must require $U_{mn}(t) = u_{mn}^2(t)$. Then equation (7) may be rewritten as follows

$$\varphi(x, y, t) = u^2(t) \cdot \phi(x, y) \quad (9)$$

A one-term shape function that satisfies the boundary conditions for w in equation (4) may be expressed as

$$W(x, y) = W = \sin \frac{\pi x}{a} \sin \frac{\pi y}{b} \quad (10)$$

Of course, there are an infinite number of such shape functions, using integer multiples of π in each direction

that could be superimposed to generalize the solution space; however, this generalized approach does not lend itself to an easily-solvable system for which a simple solution is desired for this SHM application. Such a multi-term shape function superposition would, clearly, continue to improve the accuracy of the vibration prediction, but the terms are inversely proportional to the square of the integer multiples of π, so convergence is rapidly achieved, and a one-mode solution is reasonable for the application, as experiment will bear out.

Substituting equations (9) and (10) into equation (3) yields

$$\frac{1}{E_1}\frac{\partial^4 \phi}{\partial y^4} + \frac{1}{E_2}\frac{\partial^4 \phi}{\partial x^4} = \left(\frac{\partial^2 W}{\partial x \partial y}\right)^2 - \frac{\partial^2 W}{\partial x^2}\frac{\partial^2 W}{\partial y^2} \qquad (11)$$

and substituting equation (10) into equation (11) yields

$$\frac{1}{E_1}\frac{\partial^4 \phi}{\partial y^4} + \frac{1}{E_2}\frac{\partial^4 \phi}{\partial x^4} = \frac{\pi^4}{2a^2 b^2}\left(\cos\frac{2\pi x}{a} + \cos\frac{2\pi y}{b}\right) \qquad (12)$$

From an analysis of the solution structure of equation (12) and the boundary conditions, the solution of equation (12) takes the form

$$\phi(x,y) = \alpha \cdot \cos\frac{2\pi x}{a} + \beta \cdot \cos\frac{2\pi y}{b} + \gamma_1 x^3$$
$$+ \gamma_2 y^3 + \gamma_3 x^2 y + \gamma_4 xy^2 + \gamma_5 x^2 + \gamma_6 y^2 + \gamma_7 xy \qquad (13)$$

Substituting equation (13) into equation (12) yields

$$\frac{16\pi^4 \alpha}{a^4 E_2}\cos\frac{2\pi x}{a} + \frac{16\pi^4 \beta}{b^4 E_1}\cos\frac{2\pi y}{a}$$
$$= \frac{\pi^4}{2a^2 b^2}\left(\cos\frac{2\pi x}{a} + \cos\frac{2\pi y}{b}\right) \qquad (14)$$

and from equation (14), we obtain the relationships

$$\alpha = \frac{E_2 a^2}{32 m^2 b^2}, \beta = \frac{E_1 b^2}{32 n^2 a^2}$$

Substituting equation (13) into boundary conditions (5) yields

$$\begin{cases}
\frac{\partial^2 \phi}{\partial x^2}(0,y,t) = 2\gamma_3 y + 2\gamma_5 - \alpha\frac{4\pi^2}{a^2} = 0 \\
\frac{\partial^2 \phi}{\partial x^2}(a,y,t) = 6\gamma_1 a + 2\gamma_3 y + 2\gamma_5 - \alpha\frac{4\pi^2}{a^2} = 0 \\
\frac{\partial^2 \phi}{\partial y^2}(x,0,t) = 2\gamma_4 x + 2\gamma_6 - \beta\frac{4\pi^2}{b^2} = 0 \\
\frac{\partial^2 \phi}{\partial y^2}(x,b,t) = 6\gamma_2 b + 2\gamma_4 x + 2\gamma_6 - \beta\frac{4\pi^2}{b^2} = 0 \\
\frac{\partial^2 \phi}{\partial x \partial y} = \gamma_7 = 0
\end{cases}
\Rightarrow
\begin{cases}
\gamma_1 = \gamma_2 = \gamma_3 = \gamma_4 = \gamma_7 = 0 \\
\gamma_5 = \frac{\pi^2 E_2}{16 b^2} \\
\gamma_6 = \frac{\pi^2 E_1}{16 a^2}
\end{cases}$$

Substituting α, β, γ_1, γ_2, γ_3, γ_4, γ_5, γ_6, γ_7 into equation (13) and then substituting equation (13) into equation (9) yield

$$\varphi(x,y,t) =$$
$$\left(\frac{E_2 a^2}{32 b^2}\cos\frac{2\pi x}{a} + \frac{E_1 b^2}{32 a^2}\cos\frac{2\pi y}{b} + \frac{\pi^2 E_2}{16 b^2}x^2 + \frac{\pi^2 E_1}{16 a^2}y^2\right)u^2(t) \qquad (15)$$

Substituting equations (10), (11), and (17) into equation (2) and invoking Galerkin's method, we have

$$\iint_S \left[\frac{\rho}{h}\frac{\partial^2 w}{\partial t^2} - \left(\sigma_{0x} + \frac{\partial^2 \varphi}{\partial y^2}\right)\frac{\partial^2 w}{\partial x^2} - \left(\sigma_{0y} + \frac{\partial^2 \varphi}{\partial x^2}\right)\frac{\partial^2 w}{\partial y^2}\right]W ds$$
$$+ \iint_S \left[\frac{\rho}{h}W\frac{\partial^2 u(t)}{\partial t^2} - \left(\sigma_{0x}\cdot\frac{\partial^2 W}{\partial x^2} + \sigma_{0y}\cdot\frac{\partial^2 W}{\partial y^2}\right)u(t)\right.$$
$$\left. - \left(\frac{\partial^2 W}{\partial x^2}\frac{\partial^2 \phi}{\partial y^2} + \frac{\partial^2 W}{\partial y^2}\frac{\partial^2 \phi}{\partial x^2}\right)u^3(t)\right]W ds = 0 \qquad (16)$$

Performing the domain integrations in equation (16) leads to a nonlinear differential equation with respect to $u(t)$

$$\xi_1 \cdot \frac{d^2 u(t)}{dt^2} + \xi_2 \cdot u(t) + \xi_3 \cdot u^3(t) = 0 \qquad (17)$$

where

$$\xi_1 = \iint_S \frac{\rho}{h}W^2 ds = \iint_S \frac{\rho}{h}\sin^2\frac{\pi x}{a}\sin^2\frac{\pi y}{b}ds = \frac{\rho ab}{4h}$$

$$\xi_2 = -\iint_S \left(\sigma_{0x}\cdot\frac{\partial^2 W}{\partial x^2} + \sigma_{0y}\cdot\frac{\partial^2 W}{\partial y^2}\right)W ds = \frac{\pi^2 ab}{4}\left(\frac{\sigma_{0x}}{a^2} + \frac{\sigma_{0y}}{b^2}\right)$$

$$\xi_3 = -\iint_S \left(\frac{\partial^2 W}{\partial x^2}\frac{\partial^2 \phi}{\partial y^2} + \frac{\partial^2 W}{\partial y^2}\frac{\partial^2 \phi}{\partial x^2}\right)W ds = \frac{3ab\pi^4}{64}\left(\frac{E_1}{a^4} + \frac{E_2}{b^4}\right)$$

By substituting the values of ξ_1, ξ_2, and ξ_3 into equation (17), we obtain

$$\frac{d^2u(t)}{dt^2} + \frac{h\pi^2}{\rho}\left(\frac{\sigma_{0x}}{a^2} + \frac{\sigma_{0y}}{b^2}\right)u(t) + \frac{3h\pi^4}{16\rho}\left(\frac{E_1}{a^4} + \frac{E_2}{b^4}\right)u^3(t) = 0$$

By setting $\lambda = h\pi^2/\rho((\sigma_{0x}/a^2) + (\sigma_{0y}/b^2))$ and $\varepsilon = 3h\pi^4/16\rho((E_1/a^4) + (E_2/b^4))$, we then have

$$\frac{d^2u(t)}{dt^2} + \lambda \cdot u(t) + \varepsilon \cdot u^3(t) = 0 \tag{18}$$

By multiplying equation (18) through by $2\dot{u}(t)$ and integrating, we obtain

$$\left(\frac{du(t)}{dt}\right)^2 + \lambda \cdot u^2(t) + \frac{\varepsilon}{2} \cdot u^4(t) = C \tag{19}$$

where C is determined by the initial conditions. Once the inelastic collision has completed, we assume that the initial displacement is $u(t)|_{t=0} = u_{\max}$, where the membrane has maximal strain energy, and that the corresponding velocity is

$$\left.\frac{du(t)}{dt}\right|_{t=0} = 0$$

The substitution of $u(t)|_{t=0} = u_{\max}$ and

$$\left.\frac{du(t)}{dt}\right|_{t=0} = 0$$

into equation (19) yields

$$C = \lambda \cdot u_{\max}^2 + \frac{\varepsilon}{2}u_{\max}^4 \tag{20}$$

Conversely, at the initiation of the collision, if we assume that the initial velocity is

$$\left.\frac{du(t)}{dt}\right|_{t=0} = v_{\max}$$

when the membrane is at the equilibrium position, the initial displacement is $u(t)|_{t=0} = 0$. The substitution of

$$\left.\frac{du(t)}{dt}\right|_{t=0} = v_{\max}$$

and $u(t)|_{t=0} = 0$ into equation (1) yields

$$C = v_{\max}^2 \tag{21}$$

In such inelastic conditions, energy is not conserved in general, but there is elasticity in the membrane that can absorb the initial kinetic energy, we assume the substantive majority of that kinetic energy is transferred therein to elastic potential energy, although we acknowledge some energy is clearly converted to heat or sound due to the pellet/membrane interaction. With this assumption, equations (20) and (21) are equated, yielding

$$\lambda \cdot u_{\max}^2 + \frac{\varepsilon}{2}u_{\max}^4 = v_{\max}^2 \tag{22}$$

When the pellet impacts onto the center of the membrane surface, the pellet and the center point of the membrane will move together at the velocity of $v_{\max}$ in accordance with the inelastic collision model. The velocity distribution is assumed to scale spatially from the maximum at the impact point to zero at the boundaries, consistent with the boundary conditions, according to

$$v(x,y) = \begin{cases} v_{\max} \cdot \dfrac{4}{ab}xy, & (0 \leqslant x \leqslant a/2, 0 \leqslant y \leqslant b/2) \\[2mm] v_{\max} \cdot \dfrac{4}{ab}(a-x)(b-y), & (a/2 \leqslant x \leqslant a, b/2 \leqslant y \leqslant b) \\[2mm] v_{\max} \cdot \dfrac{4}{ab}x(b-y), & (0 \leqslant x \leqslant a/2, b/2 \leqslant y \leqslant b) \\[2mm] v_{\max} \cdot \dfrac{4}{ab}(a-x)y, & (a/2 \leqslant x \leqslant a, 0 \leqslant y \leqslant b/2) \end{cases} \tag{23}$$

where $v(x,y)$ is the distribution function of velocity of the membrane when the pellet just hits the center of the membrane. This function was chosen because it satisfies boundary conditions, scales appropriately, and gives reasonable results in the final prediction formula.

While energy is not strictly conserved, momentum is conserved, and applying a momentum balance (exploiting the symmetry of the velocity distribution function), we obtain the following expression (24)

$$Mv_0 = M \cdot v_{\max} + 4\int_0^{\frac{a}{2}}\int_0^{\frac{b}{2}} \rho \cdot v_{\max} \cdot \frac{4xy}{ab}dxdy \tag{24}$$

where M is the mass of the pellet and v_0 is the initial velocity of the pellet. By solving equation (24), we find

$$v_{\max} = \frac{4Mv_0}{4M + \rho ab} \tag{25}$$

The substitution of λ, ε, and equation (25) into equation (22) yields

$$\frac{\pi^2}{\rho}\left(\frac{N_{0x}}{a^2} + \frac{N_{0y}}{b^2}\right) \cdot u_{\max}^2 + \frac{3h\pi^4}{32\rho}\left(\frac{E_1}{a^4} + \frac{E_2}{b^4}\right) \cdot u_{\max}^4 = \left(\frac{4Mv_0}{4M + \rho ab}\right)^2 \tag{26}$$

where $N_{0x} = h \cdot \sigma_{0x}$ and $N_{0y} = h \cdot \sigma_{0y}$. Generally, the pretension in x and y directions are equal, namely $N_{0x} = N_{0y} = N_c$, and so equation (26) becomes in final form

Table 1. Parameters of three kinds of membrane material.

Type	Heytex H5573	Xing Yi Da	ZZF 3010
Area density	270 g/m^2	1050 g/m^2	950 g/m^2
Thickness	0.80 mm	0.82 mm	0.72 mm
Tensile strength (warp/weft)	4400/4200 N/5 cm	5500/5000 N/5 cm	4000/3700 N/5 cm
Young's modulus (warp/weft)	1720/1490 MPa	1520/1290 MPa	1590/1360 MPa
Extreme temperature	−30°C to +70°C	−30°C to +70°C	−30°C to +70°C
Transmittance	8%	7%	8%

$$\frac{\pi^2 N_c}{\rho}\left(\frac{1}{a^2}+\frac{1}{b^2}\right)\cdot u_{max}^2 + \frac{3h\pi^4}{32\rho}\left(\frac{E_1}{a^4}+\frac{E_2}{b^4}\right)\cdot u_{max}^4$$
$$=\left(\frac{4Mv_0}{4M+\rho ab}\right)^2 \tag{27}$$

Equation (27) is the formula for detecting the pretension of the membrane structure. The only unknown parameters are u_{max}, which is obtained from measurement, and N_c, which is the desired target parameter that will be estimated from equation (27). For the whole membrane surface, the detecting area is a relatively small area. So we can consider the measurement area is a plane area, although the whole membrane surface is curved. In order to obtain u_{max}, we launch a pellet to impact the center point of the membrane and measure the response by a laser displacement sensor. Then maximum amplitude is substituted into equation (27), which is solved to obtain the pretension of the membrane.

Experimental verification

This section will describe experimental validation of the method proposed in the previous section.

Experimental testbed description

In order to stretch the membrane specimens, a tensioning device was designed as shown in Figure 2. The whole plane size of this stretching device is 3800 mm × 4160 mm, the center area size is 1200 mm × 1200 mm, and the height is 1600 mm. The stretching device is welded together by a 60 mm × 60 mm square steel tube, and an M20 screw is used to stretch it.

The schematic of the entire experimental application is shown in Figure 3. In this experiment, we used a gun to shoot steel, glass, and plastic pellets onto the membrane surface to excite the membrane. The initial velocity of the pellet (v_0) is known by a velocimeter (as shown in Figure 3). The HP-10K digital display pull-and-push dynamometer (as shown in Figure 3) is applied to monitor the actual pretension of the membrane. The maximum range and minimum calibration of the HP-10K dynamometer are 10 and 0.01 kN,


Figure 2. Tensioning device.

respectively. The dynamic response of the membrane was measured with a laser displacement sensor (also as shown in Figure 3), with a maximum range of 100 mm and the sampling frequency of 2 kHz. It has RS485 serial output, trigger input, AL logic control terminal, and 5 m telemetry cable.

Experimental materials

The experiment considered three kinds of membrane material that are commonly applied in structural applications. They are Heytex H5573, ZZF 3010, and Xing Yi Da. The parameters of the three membranes are shown in Table 1. All the membrane test specimens are cross-shaped (Figure 4). The maximum size of each test specimen is 2500 mm × 2500 mm, and the size of the center area is 1200 mm × 1200 mm and 1200 mm × 800 mm. A rope is rolled in the edge of each specimen, and the edge is heat-sealed. The four overhanging parts of each specimen are lanced. The specific processing dimension of the cross-shaped membrane specimens is shown in Figure 5.
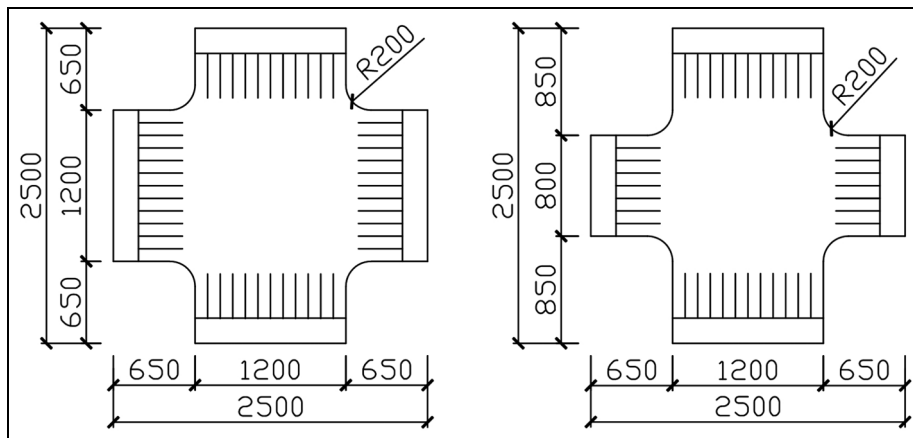
Loading profile

The uniform pretension loading pattern is divided into eight levels: 1.0, 2.0, 3.0, 4.0, 5.0, 6.0, 7.0, and 8.0 kN.
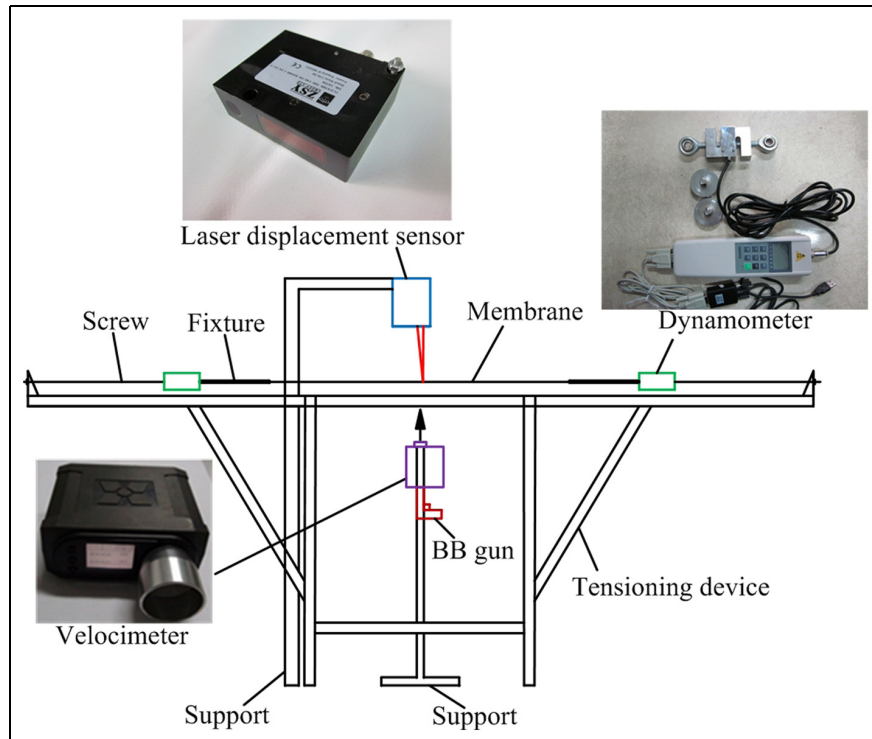
Figure 3. Schematic of the entire experimental application.

Figure 4. Photos of the cross-shaped experimental membrane specimens: Heytex square specimen (left), Xing Yi Da square specimen (center) and ZZF rectangle specimen (right).

Figure 5. Processing dimension of the square and rectangle membrane specimens.

Figure 6. Photo of the field experiment.

The membrane specimen is stretched by the tensioning device as shown in Figure 6.

The center point of the membrane surface was marked and the pellets were launched respectively onto the center point of the membrane surface under different pretension levels. The gun is fixed under the tensioned membrane plane, and the incident direction is perpendicular to the membrane surface. The laser displacement sensor is fixed above the tensioned membrane surface to monitor the dynamic responses of the impact point as shown in Figure 6.

Experimental procedure

The initial velocities of the pellets were calibrated before the experiment. All the calibrated velocities are the average velocities of eight tests. The calibration results and other basic parameters are shown in Table 2.

Each experiment was conducted according to the following main steps:

1. The membrane specimens were fixed to the stretching device by fixtures, dynamometer, and screws, and then the laser displacement sensor was fixed above the membrane specimen by steel supports.
2. The screw rods were tensioned to apply horizontal loads (starting from the lowest level: 1.0 kN or 1.0 kN: 2.0 kN) until the dynamometer reached the target load level. At the same time, rulers were used to measure the distance between the center point of the membrane plane and the four borders of the tensioning device to ensure the center point of the membrane plane coincides with the center of the stretching device.
3. The gun was fixed under the positioning device and vertically aligned to the center point of the membrane plane. At the same time, the laser displacement sensor was turned on that is connected to the computer.

Table 2. Basic parameters of the three kinds of pellets.

Parameters	Weight (g)	Diameter (mm)	Initial velocity v_0 (m/s)
Steel	0.88	6	15.78
Glass	0.25	6	41.00
Plastic	0.14	6	73.37

4. The pellet was shot to the center point of the membrane surface, and the laser displacement sensor recorded and saved the response data at the impact point. Each pellet was shot three times under each pretension level, and we took the averages to accommodate some inevitable uncertainty or external influences.
5. The process was repeated for the next pellet.
6. The screw rods were adjusted to increase the pretension to the other pretension levels and then repeated the above steps.

Experimental results and discussion

The maximum amplitudes (u_{max}) of the center point of the three membrane specimens under different pretension levels are shown in Tables 3 to 5. In Tables 3 to 5, SP denotes steel pellet, GP denotes glass pellet, and PP denotes plastic pellet.

Substituting each u_{max}, the material parameters of membrane specimens, and the pellets parameters into equation (27), it was solved to obtain the computational pretensions: N_{cs} (computed by the impact of steel pellet), N_{cg} (computed by the impact of glass pellet), and N_{cp} (computed by the impact of plastic pellet). The corresponding actual pretension N_a is the pretension level. The computational and actual pretensions are shown in Tables 6 to 8 and Figures 7 to 9. We define the relative differences between computational and actual pretensions by:

$$\text{Das} = \frac{N_{cs} - N_a}{N_a} \times 100\%$$

$$\text{Dag} = \frac{N_{cg} - N_a}{N_a} \times 100\% \qquad (28)$$

$$\text{Dap} = \frac{N_{cp} - N_a}{N_a} \times 100\%$$

where Das denotes relative difference between N_a and N_{cs}, Dag denotes relative difference between N_a and N_{cg}, and Dap denotes relative difference between N_a and N_{cp}. According to equation (28), the relative differences between computational and actual pretensions are computed and shown in Tables 9 to 11, and their

Table 3. Maximum amplitudes of the center point of square Xing Yi Da membrane.

N_a (kN)	1	2	3	4	5	6	7	8
u_{max} (SP) (mm)	0.3427	0.2475	0.2014	0.1725	0.1553	0.1388	0.1263	0.1159
u_{max} (GP) (mm)	0.2662	0.1882	0.1532	0.1322	0.1176	0.1065	0.0985	0.0913
u_{max} (PP) (mm)	0.2631	0.1853	0.1491	0.1292	0.1152	0.1052	0.0955	0.0874

SP: steel pellet; GP: glass pellet; PP: plastic pellet.

Table 4. Maximum amplitudes of the center point of square Heytex membrane.

N_a (kN)	1	2	3	4	5	6	7	8
u_{max} (SP) (mm)	0.5978	0.4290	0.3540	0.3078	0.2747	0.2533	0.2356	0.2208
u_{max} (GP) (mm)	0.4316	0.3135	0.2589	0.2236	0.2046	0.1881	0.1737	0.1642
u_{max} (PP) (mm)	0.4336	0.3122	0.2637	0.2312	0.2068	0.1877	0.1743	0.1631

SP: steel pellet; GP: glass pellet; PP: plastic pellet.

Table 5. Maximum amplitudes of the center point of rectangle ZZF membrane.

N_a (kN)	1	2	3	4	5	6	7	8
u_{max} (SP) (mm)	0.4332	0.3011	0.2389	0.2018	0.1826	0.1667	0.1556	0.1436
u_{max} (GP) (mm)	0.3341	0.2286	0.1856	0.1637	0.1458	0.1301	0.1208	0.1101
u_{max} (PP) (mm)	0.3245	0.2267	0.1843	0.1587	0.1434	0.1278	0.1188	0.1098

SP: steel pellet; GP: glass pellet; PP: plastic pellet.

Table 6. Comparison between computational and actual pretensions of square Xing Yi Da membrane.

N_a (kN)	1	2	3	4	5	6	7	8
N_{cs} (kN)	0.842	1.680	2.536	3.458	4.266	5.341	6.450	7.660
N_{cg} (kN)	0.793	1.588	2.397	3.218	4.067	4.959	5.797	6.748
N_{cp} (kN)	0.816	1.646	2.542	3.386	4.258	5.107	6.197	7.399
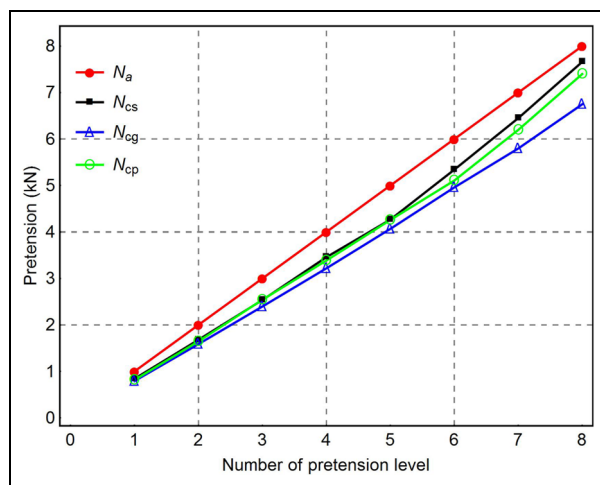
Figure 7. Actual and computational pretensions of square Xing Yi Da membrane.
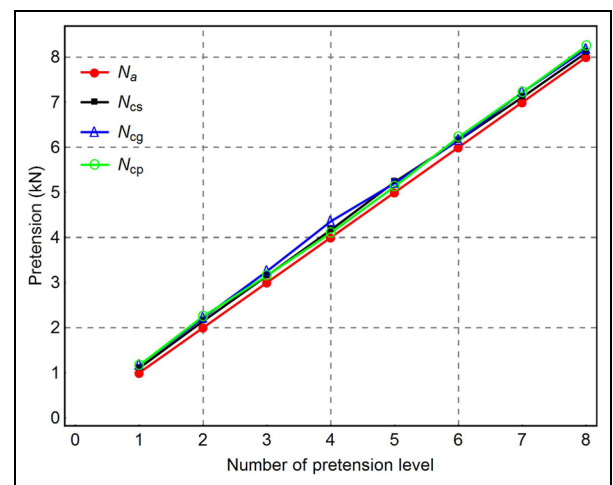
Figure 8. Actual and computational pretensions of square Heytex membrane.

Table 7. Comparison between computational and actual pretensions for square Heytex membrane.

N_a (N)	1	2	3	4	5	6	7	8
N_{cs} (kN)	1.104	2.145	3.150	4.167	5.232	6.154	7.113	8.099
N_{cg} (kN)	1.169	2.217	3.251	4.358	5.205	6.158	7.222	8.181
N_{cp} (kN)	1.166	2.250	3.154	4.103	5.129	6.225	7.220	8.245

**Table 8.** Comparison between computational and actual pretensions of rectangular ZZF membrane.

N_a (N)	1	2	3	4	5	6	7	8
N_{cs} (kN)	0.836	1.731	2.751	3.854	4.708	5.649	6.484	7.613
N_{cg} (kN)	0.770	1.646	2.497	3.209	4.046	5.081	5.893	7.095
N_{cp} (kN)	0.821	1.682	2.545	3.433	4.204	5.293	6.126	7.171

Table 9. Relative differences between computational and actual pretensions in square Xing Yi Da membrane.

Pretension level	1	2	3	4	5	6	7	8
Das (%)	−15.80	−16.00	−15.47	−13.55	−14.68	−10.98	−6.45	−4.25
Dag (%)	−20.70	−20.60	−20.10	−19.55	−18.66	−17.35	−17.19	−15.65
Dap (%)	−18.40	−17.70	−15.27	−15.35	−14.84	−14.88	−11.47	−7.51

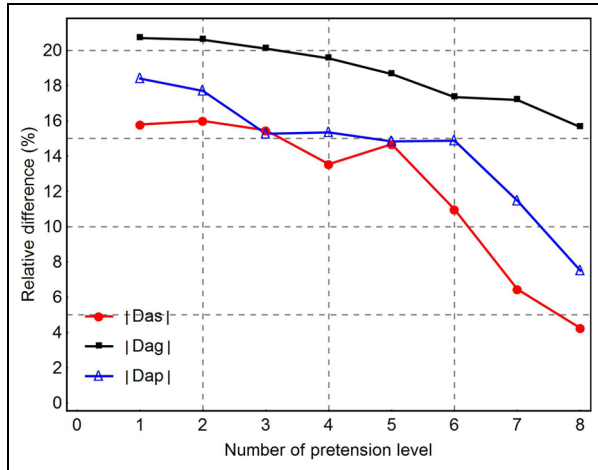**Table 10.** Relative differences between computational and actual pretensions in square Heytex membrane.

Pretension level	1	2	3	4	5	6	7	8
Das (%)	10.40	7.25	5.00	4.16	4.64	2.57	1.61	1.24
Dag (%)	16.90	10.85	8.33	8.95	4.1	2.63	3.71	2.26
Dap (%)	16.60	12.5	5.13	2.58	2.56	3.75	3.14	3.06
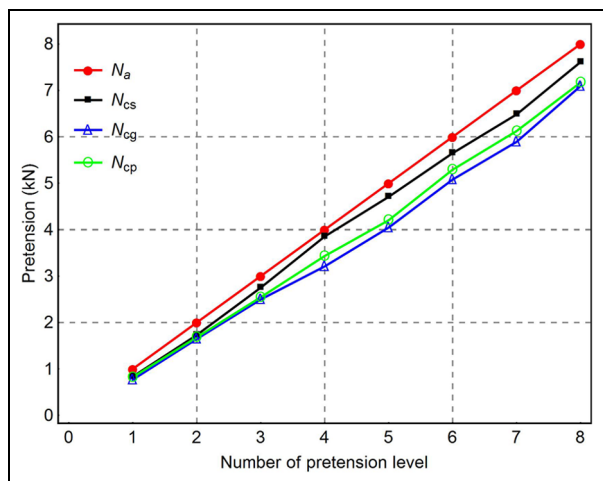
Figure 9. Actual and computational pretensions of rectangle ZZF membrane.

absolute values (|Das|, |Dag|, and |Dap|) are shown in Figures 10 to 12.

From Tables 6 to 8 and Figures 7 to 9, we can draw that the computational pretensions basically tally with their corresponding actual pretensions. For the Xing Yi Da and ZZF membrane specimens, each computational pretension is less than its corresponding actual pretension; the N_{cs} is the closest to N_a, the N_{cg} is the farthest away from N_a, and the N_{cp} is in between. For the Heytex membrane specimen, each computational pretension is larger than its corresponding actual pretension; the N_{cs} is the closest to N_a, the N_{cg} and N_{cp} have intersections, and they are all larger than N_{cs}.

From Tables 9 to 11 and Figures 10 to 12, it is clear that the absolute values of the relative difference between the actual and computational pretensions of the three specimens are all decreasing with increasing pretension levels. For the Xing Yi Da and ZZF

Figure 10. Absolute values of relative differences between actual and computational pretension in square Xing Yi Da membrane.
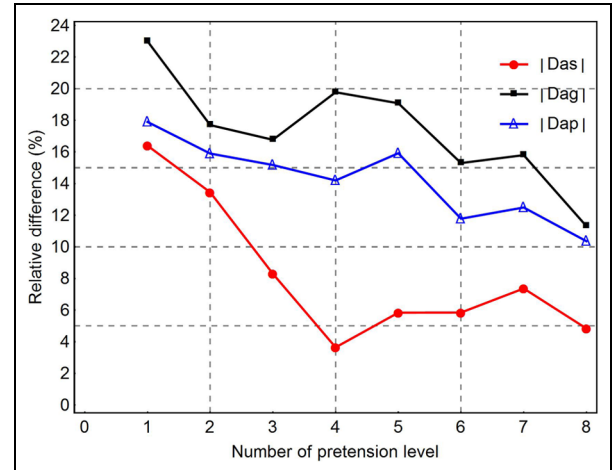
Figure 12. Absolute values of relative differences between actual and computational pretension in rectangle ZZF membrane.
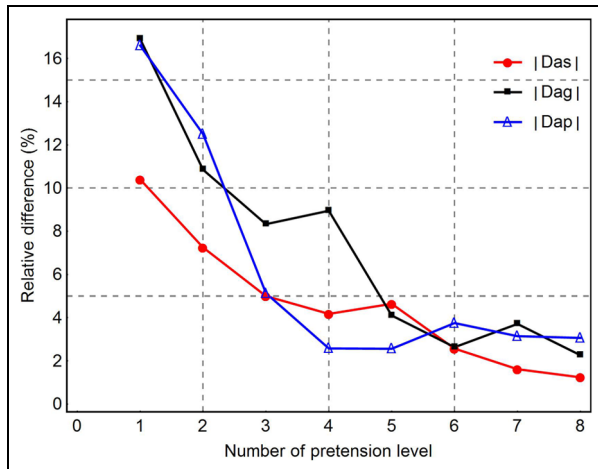
Figure 11. Absolute values of relative differences between actual and computational pretension in square Heytex membrane.

membrane specimens, the |Das| is the lowest, |Dag| is the largest, and |Dap| is in the middle. For the Xing Yi Da specimen, the largest absolute value of relative difference is 20.70% in |Dag|, and the lowest absolute value of relative difference is 4.25% in |Das|. For the ZZF specimen, the largest absolute value of relative difference is 23.00% in |Dag|, and the lowest absolute value of relative difference is 4.84% in |Das|. For the Heytex membrane specimen, the |Das|, |Dag|, and |Dap| have intersection, but the |Das| is lower than |Dag| and |Dap| in general; the largest absolute value of relative difference is 16.90% in |Dag| and the lowest absolute value of relative difference is 1.24% in |Das|; when the pretension level is >3 kN, relative differences in |Das| are all less than 5.00%.

In summary, the majority of the computational pretensions generally correlates with their corresponding actual pretensions. This verifies that the theoretical study is feasible and correct even using a relatively simple one-term shape function in the prediction model. The theoretical detection formula is more accurate for the Heytex membrane. To some extent, this reflects that the theoretical detection formula is more suitable for membranes with relative lower aerial density. The computational pretension N_{cs} that is estimated by the impact of a steel pellet is more accurate than the other two kinds of computational pretension N_{cg} and N_{cp} that are computed by the impact of glass and plastic pellets. To some extent, this reflects that the theoretical detection formula is more suitable for a pellet with relatively larger mass. In addition, the larger the pretension is, the more accurate the detection is.

In order to analyze the factors (in addition to pretension level N_a) that influenced the detection accuracy, we consider the average relative differences listed in Table 12. Form Table 12, we conclude that the aerial density of membrane ρ and the momentum $I = M \times v_0$ of the pellet are the main factors that influenced the results. The accuracy is the highest when the impact loading is applied by the steel pellet (the momentum is the largest). Therefore, we conclude that the steel pellet is best to carry out the detection process in engineering practice. For the aerial density of membrane, the highest accuracy will occur when $0.27 \, \text{kg/m}^2 < \rho < 0.95 \, \text{kg/m}^2$.

Conclusion

Through the theoretical and experimental study of the pretension estimation method in building membrane structures, we obtained the following conclusions:

Table 11. Relative differences between computational and actual pretensions in rectangular ZZF membrane.

Pretension level	1	2	3	4	5	6	7	8
Das (%)	−16.4	−13.45	−8.30	−3.65	−5.84	−5.85	−7.37	−4.84
Dag (%)	−23.00	−17.70	−16.77	−19.78	−19.08	−15.3	−15.80	−11.31
Dap (%)	−17.9	−15.90	−15.18	−14.20	−15.92	−11.78	−12.49	−10.36

Table 12. Average relative differences of different membranes under the impact of different pellets.

Pellet	Steel	Plastic	Glass
$I = M \times v_0 \ (\times 10^{-3})$ kg m/s	$0.88 \times 15.78 = 13.89$	$0.14 \times 73.37 = 10.27$	$0.25 \times 41.00 = 10.25$
Average relative differences	Das (%)	Dap (%)	Dag (%)
Heytex $\rho = 0.27$ kg/m²	4.61	6.165	7.22
ZZF $\rho = 0.95$ kg/m²	−8.21	−14.22	−17.34
Xing Yi Da $\rho = 1.05$ kg/m²	−12.15	−14.43	−18.73

1. Based on the study of the nonlinear vibration of the orthotropic rectangular membrane structure, we developed a nondestructive on-line detection method that requires only measurement of the maximum response amplitude u_{max} of the membrane to obtain the actual pretension of the building membrane structure.
2. From the experiments of the three membrane specimens (Heytex H5573, Xing Yi Da, and ZZF 3010), we concluded that all the computational pretensions generally correlate using the one-term shape function model with their corresponding actual pretensions. This effectively verified the proposed method in this article is reasonable for estimating the pretension of building membrane structures. In addition, the larger the pretension is, the more accurate the estimation is.
3. Through the analysis of the experimental results, we conclude that in addition to pretension level, the aerial density of the membrane and the momentum of the pellet are the main factors influencing the accuracy of the detection. The precision is the highest when the impact loading is applied by the steel pellet. Therefore, we conclude that a steel pellet should be used to carry out the detection in engineering practice.

The proposed method in this article can be directly applied to detect the pretension of membrane structures in the engineering practices. This method will not damage the membrane, which is significant for health monitoring of in-service membrane structures. We can take measures to strengthen the membrane structure if the detected pretension does not tally with the designed pretension, thus prevent or reduce engineering accident.

References

1. Koch KM, Habermann KJ and Forster B. *Membrane structures: innovative building with film and fabric*. Munich: Prestel Publishing, 2004.
2. Saitoh M and Okada A. Tension and membrane structures. *J Int Assoc Shell Spat Struct* 2001; 42(135–136): 15–20.
3. Stranghöner N. Tensile membrane structures. *Steel Constr* 2015; 8(4): 221.
4. Wei D, Yang QS and Shen SZ. Study on full process experiment of full scale tensioned membrane structure. *J Build Struct* 2004; 25(2): 49–56.
5. Wang DS, Zhang WY, Fang W, et al. Design and study of an long span cable membrane structure for the Expo Axis. *J Build Struct* 2010; 31(5): 1–12.
6. Ando K, Mitsugi J and Senbokuya Y. Analyses of cable–membrane structure combined with deployable truss. *Comput Struct* 2000; 74(1): 21–39.
7. Sakamoto H, Park KC and Miyazaki Y. Evaluation of membrane structure designs using boundary web cables for uniform tensioning. *Acta Astronaut* 2007; 60(10–11): 846–857.

8. Sohn H, Farrar CR, Hemez FM, et al. *A review of structural health monitoring literature: 1996–2001*. Los Alamos, NM: Los Alamos National Laboratory, 2003.

9. Farrar CR, Doebling SW and Nix DA. Vibration–based structural damage identification. *Philos T Roy Soc A* 2001; 359(1778): 131–149.

10. Staszewski WJ, Biemans C, Boller C, et al. Impact damage detection in composite structures-recent advances. *Struct Health Monit* 2000; 754–763. CRC Press.

11. Todd MD, Johnson G and Vohra S. Progress towards deployment of brag grating-based fiber optic systems in structural monitoring applications. In: *Proceedings of the European COST F3 conference on system identification and structural health monitoring*, Madrid, 6–9 June 2000, pp. 521–530. Universidad Politécnica de Madrid.

12. Todd MD, Nichols JM, Pecora LM, et al. Vibration-based damage assessment utilizing state space geometry changes: local attractor variance ratio. *Smart Mater Struct* 2001; 10(5): 1000–1008.

13. Razi P, Esmaeel RA and Taheri F. Improvement of a vibration-based damage detection approach for health monitoring of bolted flange joints in pipelines. *Struct Health Monit* 2013; 12(3): 207–224.

14. Bao CX, Hao H and Li ZX. Vibration-based structural health monitoring of offshore pipelines: numerical and experimental study. *Struct Control Hlth* 2013; 20(5): 769–788.

15. Sakaris CS, Sakellariou JS and Fassois SD. Vibration-based damage precise localization in three-dimensional structures: single versus multiple response measurements. *Struct Health Monit* 2015; 14(3): 300–314.

16. Valdés-González J, De-la-Colina J and González-Pérez CA. Experiments for seismic damage detection of a RC frame using ambient and forced vibration records. *Struct Control Hlth* 2015; 22(2): 330–346.

17. Soyoz S and Feng MQ. Instantaneous damage detection of bridge structures and experimental verification. *Struct Control Hlth* 2008; 15(7): 958–973.

18. Kim CW, Chang KC, Kitauchi S, et al. A field experiment on a steel Gerber-truss bridge for damage detection utilizing vehicle-induced vibrations. *Struct Health Monit* 2016; 15(2): 174–192.

19. Kopsaftopoulos FP and Fassois SD. A vibration model residual-based sequential probability ratio test framework for structural health monitoring. *Struct Health Monit* 2015; 14(4): 359–381.

20. Mooney MA, Gorman PB and Gonzalez JN. Vibration-based health monitoring of earth structures. *Struct Health Monit* 2005; 4(2): 137–152.

21. Carden EP and Fanning P. Vibration based condition monitoring: a review. *Struct Health Monit* 2004; 3(4): 355–377.

22. Fan W and Qiao P. Vibration-based damage identification methods: a review and comparative study. *Struct Health Monit* 2011; 10(1): 83–111.

23. Trickey S, Todd MD, Seaver ME, et al. Geometric time-domain methods of vibration-based damage detection. In: *Proceedings of the SPIE 4702, smart nondestructive evaluation for health monitoring of structural and biological systems*, San Diego, CA, 11 June 2002, p. 113. Bellingham, WA: SPIE.

24. De Roeck G. The state-of-the-art of damage detection by vibration monitoring: the SIMCES experience. *Struct Control Hlth* 2003; 10(2): 127–134.

25. Moosavian A, Khazaee M, Ahmadi H, et al. Fault diagnosis and classification of water pump using adaptive neuro-fuzzy inference system based on vibration signals. *Struct Health Monit* 2015; 14(5): 402–410.

26. Frizzarin M, Feng MQ, Franchetti P, et al. Damage detection based on damping analysis of ambient vibration data. *Struct Control Hlth* 2010; 17(4): 368–385.

27. Caicedo JM and Dyke SJ. Experimental validation of structural health monitoring for flexible bridge structures. *Struct Control Hlth* 2005; 12(3–4): 425–443.

28. Rangaraj R, Pokale B, Banerjee A, et al. Investigations on a particle filter algorithm for crack identification in beams from vibration measurements. *Struct Control Hlth* 2015; 22(8): 1049–1067.

29. Sun ZJ, Zhang QL and Yang ZL. Preliminary study on membrane pretension measurement by numerical calculations. *Zhendong Ceshi Yu Zhenduan/J Vib Meas Diagn* 2005; 25(1): 31–35.

30. Sun ZJ and Zhang QL. Simple and convenient membrane pretension measurement and testing experiments for measuring instrument. *Zhendong Ceshi Yu Zhenduan/J Vib Meas Diagn* 2005; 25(4): 280–284.

31. Sun ZJ and Zhang QL. A study on pre-tension measurement of membrane structures. *Int J Space Struct* 2005; 20(2): 71–82.

32. Zheng ZL, Liu CJ, Gong WC, et al. A new method—ejection method for nondestructive online monitoring of the pretension of building membrane structure. *Struct Control Hlth* 2013; 20(4): 445–464.

34. Zheng ZL, Liu CJ, He XT, et al. Free vibration analysis of rectangular orthotropic membranes in large deflection. *Math Probl Eng* 2009; 2009: 634362-1–634362-9.

35. Liu CJ, Zheng ZL, Yang XY, et al. Nonlinear damped vibration of pre-stressed orthotropic membrane structure under impact loading. *Int J Struct Stab Dy* 2014; 14(1): 1350055.

36. Liu CJ, Zheng ZL, Jun L, et al. Dynamic analysis for nonlinear vibration of prestressed orthotropic membranes with viscous damping. *Int J Struct Stab Dy* 2013; 13(2): 1350018.